







Gyrokinetic simulations of magnetohydrodynamic modes in stellarator plasmas

Carolin Nührenberg¹ , R. Kleiber¹ , A. Mishchenko¹ , A. Könies¹ ,
M. Borchardt¹  and R. Hatzky² 

¹MPI Plasma Physics, 17491 Greifswald, Germany

²MPI Plasma Physics, 85748 Garching, Germany

Corresponding author: Carolin Nührenberg, carolin.nuehrenberg@ipp.mpg.de

(Received 15 November 2024; revision received 16 April 2025; accepted 17 April 2025)

For small-shear helical-axis stellarators, linear ideal-magnetohydrodynamic (MHD) stability calculations and full-torus, nonlinear, electromagnetic gyrokinetic (GK) simulations (the latter with this unprecedented combination of objectives in stellarator GKs) in their linear phase are shown to yield well agreeing spatio-temporal structures of unstable, globally extended perturbations. Likewise, good agreement is found for their dependence on the plasma pressure and the vacuum-field magnetic well in plasma equilibria with identical gradient lengths of the temperature and density profiles. In the nonlinear phase, these perturbations with MHD signatures entail deformations of the magnetic surfaces, growing magnetic islands which rotate in the electron diamagnetic direction and, eventually, lead to ergodisation of a larger part of the magnetic surfaces.

Key words: plasma instabilities, plasma simulation, fusion plasma

1. Introduction

Stellarator optimisation traditionally used (Nührenberg *et al.* 1993) and still uses (Drevlak *et al.* 2018) ideal magnetohydrodynamic (MHD) proxies such as the vacuum-field magnetic well to ensure stability of the plasma equilibria. This property prevails in an ideal-MHD equilibrium if the toroidal magnetic flux, F_T , enclosed by a sequence of magnetic surfaces between the magnetic axis and plasma edge increases more strongly than the corresponding enclosed volume, i.e. $d^2V/dF_T^2 < 0$. Already in Bernstein *et al.* (1958), on the energy principle of MHD stability, this quantity appears as a sufficient condition for the instability of an axisymmetric system. Deepening the vacuum-field magnetic well comes at the expense of the plasma shape, resulting in more complex magnet systems. Since, on the one hand, the stability of a fusion plasma is indispensable for good confinement and, on the other hand, economical coil design is a key ingredient for the success of future stellarator devices, the importance of the concept of a vacuum-field magnetic well is assessed in the present work.

The work presented here studied helical-axis stellarator configurations that lack stabilisation by a vacuum-field magnetic well. In addition, unlike other studies, a broader physical picture was chosen to highlight the differences and similarities between linear ideal-MHD and gyrokinetics (GK). It is well known that the reduced-MHD equations can be derived from gyrofluid equations (Brizard 1992) and, furthermore, that there is a significant correlation between reduced MHD and nonlinear GK (Brizard & Hahm 2007). Moreover, in nonlinear GK, turbulent and large-scale structures regulate each other. This indicates that it is crucial to master the MHD-limit scenario as a prerequisite for high-fidelity GK turbulence simulations. Furthermore, it is still an open question if the stability limit given by ideal-MHD is decisively influenced by GK effects.

Examples of stellarator MHD stability studies have earlier been published by Ramasamy *et al.* (2024) and Zhou *et al.* (2024). In the former global, nonlinear, reduced-MHD and linear-MHD calculations were done using the JOREK and CASTOR3D codes in applications studying the W7-AS stellarator. The latter discusses nonlinear resistive MHD calculations done with the M3D – C1 code focusing on the optimised stellarator Wendelstein 7-X (W7-X).

In tokamak research, many authors discuss the relationship of the fields of MHD and GK. An example is the work of Brochard *et al.* (2022) who describe a linear verification of the GK GTC code against kinetic-MHD codes in the ideal-MHD limit studying internal kink modes in the DIII-D tokamak. An equivalent study for pressure-driven modes in stellarators has not yet been provided and is therefore one of the aims of the present work.

Currently, only a few codes are able to perform the complex task of global, GK simulations in stellarator scenarios, among them GENE – 3D (Wilms *et al.* 2024), XGC – S (Cole *et al.* 2019) and EUTERPE (Kleiber *et al.* 2024). The latter two fall in the category of Lagrangian particle-in-cell (PIC) codes, while GENE – 3D is grid-based and uses an Eulerian description.

Given that low-mode-number perturbations have the potential to impact a large plasma volume, they are the subject of this study. Therefore, the simulations need to be full radius (magnetic axis to plasma boundary) and full torus (including all field periods of the configuration). The nonlinear, electromagnetic EUTERPE simulations presented below combine this geometrical set-up and the usage of kinetic ions and electrons at a realistic mass ratio. To the authors' best knowledge, it is the first time that this combination of objectives was achieved in GK simulations for a stellarator scenario.

The paper is structured as follows. The description of the plasma equilibria is followed by brief overviews on the models and methods used in the MHD-stability and GK calculations. Details of the numerical set-up are given in § 5. In the first part of § 6, a comparison of linear-ideal-MHD stability and linear-phase nonlinear GK simulations is given, followed, in the second part, by a discussion of points specific to the GK simulations such as zonal components and the evolution of islands. Finally, a summary with conclusions and an outlook are given.

2. Description of equilibria

The Wendelstein 7-X configuration space was developed on the basis of the so-called HELIAS concept (Nührenberg & Zille 1986; Beidler *et al.* 1990). In the present work, the object of study are sequences of HELIAS configurations, i.e. helical-axis stellarators, with either the vacuum-field magnetic well or the volume-averaged plasma- β chosen as scan parameter. (Throughout this paper, β denotes

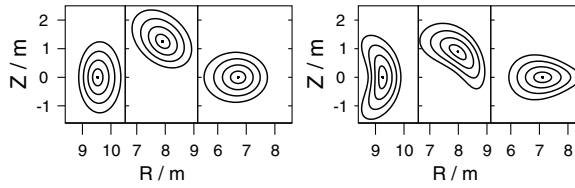


FIGURE 1. Cross-sections of helical-axis stellarators shown at the beginning, at a quarter and at the middle of a field period. Left: turning-ellipse plasma boundary, right: HELIAS configuration with indentation and triangularity. Only five of the total of 800 magnetic surfaces are shown.

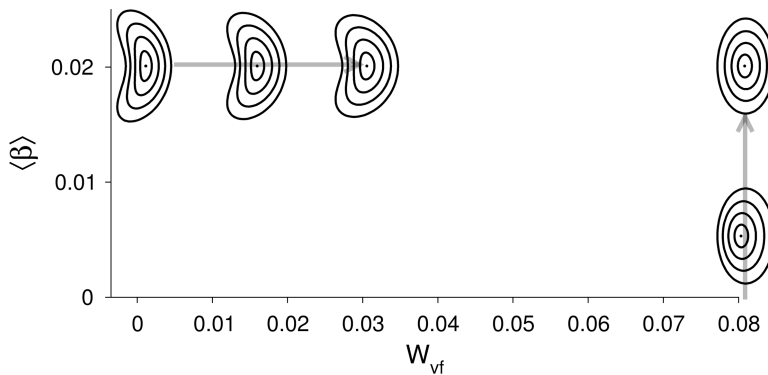


FIGURE 2. Overview of the equilibrium sequences and their dependency on the vacuum-field magnetic anti-well (W_{vf}) and the volume-averaged plasma- β . Only the $\varphi = 0^\circ$ cross-sections are shown for five of the in total eleven equilibria. Compare [figure 1](#) for more cross-sections.

the ratio of the flux-surface averages of the plasma and the magnetic pressures; $\langle\beta\rangle$ stands for the respective volume average.) [Figure 1](#) shows the variation of the plasma cross-sections in half a field period for the simplest and for the geometrically most demanding cases, while [figure 2](#) gives an overview of the equilibrium sequences by showing the $\varphi = 0^\circ$ cross-sections of five exemplary cases. The simplest case is a so-called $\ell = 1, 2$ stellarator with turning-ellipse cross-sections. It is used to study the influence of an increasing plasma pressure. Keeping the plasma pressure fixed, the second sequence of equilibria allows us to study the effect of boundary shaping and the vacuum-field magnetic well. Going to the more strongly shaped configurations, the plasma boundaries exhibit simultaneously increasing indentation, ellipticity and triangularity. The description of the plasma boundaries for all of the cases is given in [Appendix A](#). For the $\ell = 1, 2$ case, the helical excursion of the magnetic axis is roughly the size of the minor radius (denoted by a) vertically and $1.5a$ horizontally. Therefore, even the $\ell = 1, 2$ case has, on the one hand, enough geometrical and, hence, magnetic-field complexity to be a meaningful object of study, but is, on the other hand, simple enough as a test bed.

In the following, the normalised toroidal flux, s , is used as flux label with $s = 0$ at the magnetic axis and $s = 1$ at the plasma boundary. Primes denote derivatives with respect to s for functions that are constant on magnetic surfaces. With V the contained volume of a magnetic surface with flux label s , $V'' < 0$ prevails in an equilibrium with a magnetic well, because then the enclosed volume increases less strongly than the enclosed toroidal flux. On the other hand, a magnetic hill,

$V'' > 0$, implies that the contained volume increases faster than the flux, i.e. that the magnetic field weakens in the outer regions (Greene 1997). The magnetic well present in a vacuum field is further deepened by the plasma pressure in the case of finite plasma- β . Therefore, the vacuum-field magnetic well is an important proxy for ideal-MHD stability (Mercier 1962) in low-shear, net-current-free stellarators. Obviously, the pressure profile and the equilibrium must be consistent. For the series of equilibria with fixed plasma pressure and varying relative vacuum-field magnetic-well depth \mathcal{W}_{vf}

$$\mathcal{W}_{\text{vf}} = \frac{V'(1) - V'(0)}{V'(0)} \quad (2.1)$$

ranges from a marginal magnetic well, $\mathcal{W}_{\text{vf}} = -0.002$, to a moderate magnetic anti-well or hill, $\mathcal{W}_{\text{vf}} = 0.03$.

The $\ell = 1, 2$ equilibria have a constant high vacuum-field magnetic-field anti-well ($\mathcal{W}_{\text{vf}} = 0.08$), so are more unstable to MHD; these are used for a stability scan in plasma- β . In stellarators the variation of the magnetic-field strength on the magnetic axis (with the minimum B_{min} and the maximum B_{max} , here given as a relative mirror ratio)

$$\mathcal{M}_{\text{B}} = \frac{B_{\text{max}} - B_{\text{min}}}{2 B_{\text{av}}}, \quad (2.2)$$

may be more or less pronounced; in ideal axisymmetric tokamaks it is zero. The strength of the magnetic mirror is also seen in the respective Fourier component of the magnetic-field strength, e.g. B_{01} in the right panel of figure 3. For the HELIAS cases, the magnetic mirror ratio increases with increasing vacuum-field magnetic hill from $\mathcal{M}_{\text{B}} = 0.014$ to ≈ 0.07 . To put these numbers into context, it is useful to recall that, as a consequence of the optimisation, nearly all W7-X configurations have a vacuum-field magnetic well, e.g. $\mathcal{W}_{\text{vf}} \approx -0.01$ for the W7-X standard case, which has a mirror ratio of $\mathcal{M}_{\text{B}} \approx 0.05$ (Dinklage *et al.* 2018). An exception is the low- ι very-high-mirror W7-X with $\mathcal{W}_{\text{vf}} \approx 0.0044$ and $\mathcal{M}_{\text{B}} \approx 0.25$.

Without much loss of generality, the so-called stellarator symmetry (Dewar & Hudson 1998) is employed, which is analogous to the consideration of an up-down symmetric tokamak. Furthermore, the plasma domain is chosen to have a fourfold discrete symmetry, i.e. to consist of four identical field periods, $N_{\text{p}} = 4$. Further equilibrium parameters are the major and minor radii of $R_0 = 8$ m and of $a = 1$ m, and, hence, an aspect ratio of $A = R_0/a = 8$. The equilibria are calculated using the VMEC code (Hirshman *et al.* 1986), which relies on the assumption of nested flux surfaces and determines a general-geometry ideal-MHD equilibrium by minimisation of the total energy of the static plasma. All the equilibria studied in this work were calculated with 800 flux surfaces. In this way sufficient resolution is supplied, especially near the magnetic axis, which otherwise is poorly resolved because VMEC uses the normalised toroidal flux as the radial coordinate. A vanishing net toroidal current is prescribed for the equilibrium calculations, as is characteristic of stellarators without a boot-strap current. This, in turn, determines the magnetic-field-line twist or rotational transform, ι . Fixed-boundary equilibria are used, so that the total enclosed toroidal flux determines the magnetic-field strength. The stellarator nature of the equilibrium is also obvious from the dominant Fourier harmonics of the magnetic-field strength B , shown by way of example for the $\ell = 1, 2$ case in the right panel of figure 3. The surface-average $B_{0,0}$, shown with its value on axis subtracted, is approximately unity with a variation of $\approx \pm 0.003$ for $\langle \beta \rangle = 0.006$. For this case, the main helical component is stronger than the term describing the axisymmetric toroidicity, and the magnetic mirror field stronger than the tokamak ellipticity term.

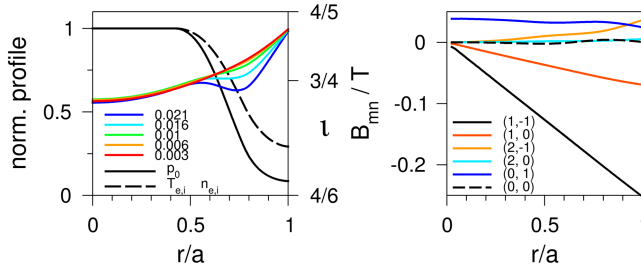


FIGURE 3. Left: equilibrium profiles versus normalised effective minor radius, r/a , for the $\ell = 1, 2$ case (left panel of figure 1): temperatures, densities (black dashed), pressure (black solid), all normalised to their axis value; rotational-transform profiles for $0.003 \leq \langle \beta \rangle \leq 0.021$ (red to blue, right-side axis). Right: Fourier spectrum of B in magnetic coordinates versus r/a . Only the dominant harmonics are shown, they are: $(m, n) = (0, 0)$ (dashed black, with its value on axis subtracted), $(1, -1)$ (main helical term, black), $(1, 0)$ (axisymmetric torus term, red), $(2, -1)$ (orange), $(0, 1)$ (mirror field, blue) and $(2, 0)$ (axisymmetric ellipticity, cyan).

Finite-pressure equilibria are obtained with the normalised pressure profile shown in the left panel of figure 3. Identical profiles are used for the normalised ion and electron temperature (T) and normalised density (n) profiles (defining the normalised equilibrium pressure p_0)

$$T_{i,e}/T_{i,e,axis} = n_{i,e}/n_{i,e,axis} = \sqrt{p_0/p_{0,axis}}. \quad (2.3)$$

Furthermore, $T_{i,axis} = T_{e,axis}$ is chosen, and it is $n_{i,axis} = n_{e,axis}$ in consequence of the assumed quasi-neutrality. With this setting the ratio of the logarithmic derivatives is unity for all species, i.e.

$$\eta = \left(\frac{T'}{T} \right) / \left(\frac{n'}{n} \right) = \frac{L_n}{L_T} = 1, \quad (2.4)$$

with L_n and L_T the normalised gradient scale lengths of unperturbed density and temperature. In § 6, additionally, an equilibrium is studied with identical pressure profile, but composed of a steeper temperature and a flat-density profile. The normalised profiles, $f(s)$, are defined by a hat function, $g(s)$, viz.

$$g(s) = p_3 \max_{0 \leq s \leq 1} \left(1 - \frac{|s - p_1|}{p_2}, 0 \right), \quad \text{and} \quad \frac{1}{f} \frac{df}{ds} = g(s). \quad (2.5)$$

For the dashed profile in the left panel of figure 3, the parameters are $p_1 = 0.6$, which is the location of the maximum gradient, $p_2 = 0.85$, the width of the gradient region, $p_3 = -2.9$, the maximum of the logarithmic derivative, and $f(0) = 1$ for the normalisation. The normalised pressure is f^2 , shown by the solid, black line in the left panel of figure 3. A sequence of equilibria with the volume-averaged plasma- β as scan parameter is established by a factor of $\sqrt{\langle \beta \rangle / 0.021}$ for the densities and temperatures and a factor of $\langle \beta \rangle$ for the pressure applied to the on-axis values given in table 2, with $\langle \beta \rangle$ the needed value of the volume-averaged plasma- β . Without a plasma pressure, the rotational transform varies as $4/6 < 0.73 \lesssim \iota \lesssim 0.79 < 4/5$ in all equilibria, thus avoiding the low-order natural resonances of four-period stellarators which are in general connected to magnetic islands (Grad 1967; Boozer

1984; Waelbroeck 2009). Depending on the local steepness of the pressure profile the rotational transform locally decreases in the region of the pressure gradient (Freidberg 2014). Using the $\ell = 1, 2$ case as an example, the dependence of ι on the plasma- β is also shown in the left panel of figure 3.

The Alfvén time is often used to normalise growth rates. Defining it with the minor radius a and the average field strength at the magnetic axis B_0 as

$$\tau_A = \frac{a}{v_A} = \frac{a \sqrt{\mu_0 \rho_0}}{B_0}, \quad (2.6)$$

a value of $\approx 0.27 \mu\text{s}$ is obtained for the $\ell = 1, 2$ and the HELIAS cases, all equilibria at $\langle\beta\rangle = 0.021$.

3. Magnetohydrodynamic stability

In the following sections, perturbed quantities are indicated by a δ , e.g. the perturbed magnetic field, $\delta\mathbf{B}$, whereas \mathbf{B} stands for the unperturbed field. In the model of linearised ideal MHD, the time evolution of the Lagrangian displacement vector, $\boldsymbol{\xi}$, describes the perturbation of the equilibrium state. The linearisation of, e.g. the ideal induction equation, determines the perturbed magnetic field

$$\delta\mathbf{B} = \nabla \times (\boldsymbol{\xi} \times \mathbf{B}). \quad (3.1)$$

The work of Bernstein *et al.* (1958) and Hain *et al.* (1957), in which the time evolution of $\boldsymbol{\xi}$ is formulated in weak form

$$\int \boldsymbol{\xi}^* \cdot \mathcal{F}[\boldsymbol{\xi}] dV + \omega^2 \int \rho_0 \boldsymbol{\xi}^* \cdot \boldsymbol{\xi} dV = 0, \quad (3.2)$$

laid the basis of the field. In equation (3.2), the volume integrals extend over the plasma and, potentially, over a surrounding vacuum domain. The equilibrium mass density is ρ_0 . An asterisk superscript stands for the complex conjugate. The ideal-MHD force operator \mathcal{F} has time-independent coefficients, therefore allowing the separation of time and space dependences. Furthermore, it is Hermitian and is bounded from below. Correa-Restrepo (1978), e.g. gives an intuitive, coordinate-free formulation of the first term of equation (3.2). For ease of reading, it is repeated in Appendix B. The Hermiticity of the force operator is obvious in this representation, equation (B.1). Field-line bending and the two compression terms, namely field and fluid compression, stabilise perturbations, while the combination of equilibrium pressure gradient and curvature and the equilibrium parallel-current density are the source of pressure and current-driven instabilities.

The two MHD codes used in the present study are CAS3D (Schwab 1993) and CKA (Slaby *et al.* 2024). While the former is based on (3.2) and uses the full formalism of linearised ideal MHD, the CKA code employs the picture of reduced MHD.

4. Gyrokinetic model

In this work, the EUTERPE code is used to perform spatially global, nonlinear, electromagnetic, GK simulations with electrons and ions as kinetic species at physical mass ratio. Collision operators are available in EUTERPE, but are not included in the present study. An in-depth description of the GK model used and of the code itself are given in Kleiber *et al.* (2024), of which only a few basics are summarised

here and in [Appendices C, D and E](#). Problems inherent to PIC techniques are addressed by means of the δf -ansatz (i.e. the distribution function f is split into a time-independent part f_0 and a time-dependent part δf) and a pull-back transformation for the mitigation of the cancellation problem (Mishchenko *et al.* 2014, 2021). For the ions/electrons, f_0 is chosen as an unshifted/shifted Maxwellian distribution, so that a potentially existing equilibrium current is carried by the electrons only. For ease of reference, the equations of motion of the PIC marker particles are included in [Appendix C](#), the field equations for the perturbation quantities $\delta\Phi$, δA_{\parallel} and δB_{\parallel} are summarised in [Appendix D](#). The EUTERPE code implements a splitting technique for the scalar perturbed parallel vector potential, δA_{\parallel} , employing a symplectic and a Hamiltonian part, see equation (C.1). The perturbed magnetic field is defined as

$$\delta \mathbf{B}^{\text{GK}} = \nabla \times (\delta A_{\parallel} \mathbf{b}) + \delta B_{\parallel} \mathbf{b}, \quad (4.1)$$

i.e. using $\mathbf{b} \cdot \nabla \times \delta \mathbf{A}_{\perp} \approx \delta B_{\parallel}$. Dong *et al.* (2017), for example, describe the inclusion of the δB_{\parallel} term in the GTC code and its importance for internal current-driven perturbation in DIII-D scenarios. Joiner *et al.* (2010) discuss the role of the compressional δB_{\parallel} for various micro-turbulence modes employing results from the flux-tube-based GK code GS2. In local linear micro-stability calculations for the spherical-tokamak fusion power plant (Kennedy *et al.* 2023), inclusion of δB_{\parallel} proved essential for instability of the dominant hybrid-kinetic-ballooning modes. This is now understood to be due to strong stabilisation by $d\beta/d\rho$, taking the equilibrium close to marginal stability (Kennedy *et al.* 2024). Consequently, the latter work found that including δB_{\parallel} is not required for local instability in tokamak equilibria at lower values of $d\beta/d\rho$. In an analysis that adopts a ballooning-space approximation, Zocco *et al.* (2015) highlight the significance of δB_{\parallel} for the stability of ion-temperature-gradient-driven modes. The role of the δB_{\parallel} term for the scenario studied here is discussed in § 6.1.

For the comparison of ideal-MHD and GK results, equations are derived connecting the displacement ξ , more specifically its component normal to flux surfaces, and the perturbed potentials $\delta\Phi$ and δA_{\parallel} through their directional derivatives along the unperturbed field-line orthogonals. In the following, $\delta \mathbf{A} = \delta A_{\parallel} \mathbf{b}$ is adopted for the perturbed vector potential as it is done in the reduced-MHD model and, often, in the GK approach. Furthermore, a purely exponential growth in time with growth rate γ , $\propto \exp(\gamma t)$, is assumed. Then, from the ideal Ohm's law, $\mathbf{E} + \mathbf{v} \times \mathbf{B} = 0$, and the representation of the perturbed electric field,

$$\delta \mathbf{E} = -\nabla \delta \Phi - \partial_t \delta \mathbf{A}, \quad (4.2)$$

an equation for the perturbed electrostatic potential, $\delta\Phi$, is obtained

$$\nabla s \times \mathbf{B} \cdot \nabla \delta \Phi = \gamma B^2 \xi \cdot \nabla s, \quad (4.3)$$

with $\nabla s/|\nabla s|$ the outer unit normal of an equilibrium flux surface. Analogously, the equation for the scalar perturbed vector potential, δA_{\parallel} , reads as

$$\nabla s \times \mathbf{B} \cdot \nabla \left(\frac{\delta A_{\parallel}}{B} \right) = -\mathbf{B} \cdot \nabla (\xi \cdot \nabla s). \quad (4.4)$$

This relation is obtained by dotting $\delta \mathbf{B}^{\text{MHD}} = \nabla \times (\xi \times \mathbf{B})$ and $\delta \mathbf{B}^{\text{GK}} = \nabla \times (\delta A_{\parallel} \mathbf{b})$ with ∇s . Anticipating the results shown in [figure 6](#), the component parallel to the background magnetic field is neglected in the GK perturbed magnetic field. Equation (4.4) is then derived using vector calculus and the fact that ∇s is normal to the equilibrium magnetic field and the equilibrium current density.

5. Numerical set-up

An inspection of the ideal-MHD energy functional, equation (B.1), shows that the stabilising contributions are minimised by perturbations fulfilling the resonance condition $k_{\parallel} \approx 0$ or $m\iota + n \approx 0$, with m and n the poloidal and toroidal perturbation mode numbers. For the equilibria described in § 2 and figure 3, the low-order rational $\iota = 3/4$ is located at approximately mid-radius. Hence, perturbations that are dominated by harmonics $(m, n) = k(4, -3)$, with integer k , are near resonant. Owing to the small shear of the rotational transform (left panel of figure 3), side bands of the dominant harmonic are resonant only for large multiples k . For example, tokamak-type side bands with $(m, n) = (4k \pm 1, -3k)$ are resonant only for $k \gtrsim 5$, given the variation of the rotational transform, $0.7 < \iota < 0.8$. This is different for stellarator-type couplings, which lead to resonant side bands even for $k = 1$. Examples are the resonant harmonics $(m, n) = (4, -3)$ and $(9, -7)$, which are coupled by the $m = 5$ equilibrium helicity. Although, in the model of linear ideal MHD, perturbations with low- k have smaller growth rates than those with high- k , the present study focuses on the former, because they are spatially large scale and, therefore, can potentially harm a larger part of the plasma. With their dominant toroidal node number not a multiple of the number of field periods, $N_p = 4$, these perturbations, however, break the fourfold periodicity of the equilibrium. According to the concept of the so-called mode families (Schwab 1993) (decoupled sets of toroidal node numbers being the stellarator analogue to the fully decoupled n in the treatment of axisymmetric equilibria), the periodicity-breaking modes do not belong to the $N = 0$ mode family. This mode family is otherwise used in EUTERPE as it allows simulations to be performed on only one field period. Therefore here, regarding the toroidal direction, the entire torus is used, technically treating it as one field period.

Radial boundary conditions must be specified at the magnetic axis and at the plasma boundary. Dirichlet conditions at the plasma edge model so-called fixed-boundary modes, which leave the plasma edge unchanged. This is imposed by enforcing vanishing harmonics of the ideal-MHD normal displacement as well as of the GK potentials, $\delta\Phi$ and δA_{\parallel} , at the plasma edge. At the magnetic axis, regularity conditions have to be fulfilled, in particular to ensure that physical quantities (e.g. the perturbed electrostatic potential and the perturbed radial electric field) are single valued. In linear ideal-MHD stability, using the normalised toroidal flux s as radial coordinate, all normal displacement harmonics have to vanish at the magnetic axis: $(\xi \cdot \nabla s)_{mn} = 0$. In the GK model, analogously, $\delta\Phi_{mn} = 0$ at the magnetic axis for non-zero m . For harmonics with $m = 0$, however, a homogeneous Neumann condition applies, $d\delta\Phi_{0n}/ds = 0$, at the magnetic axis if ρ is used as the radial coordinate. In the present work these boundary conditions are used. This is in contrast to other GK studies which omit the direct neighbourhood of the radial boundaries or use so-called buffer zones, as described e.g. in the work of Wilms *et al.* (2021), or simulate only one field period (Wilms *et al.* 2024).

The Fourier expansions that approximate the scalar components of the displacement vector in CAS3D and the field quantities in EUTERPE use identical Fourier tables, which were applied in all MHD and GK simulations presented in this work. For each toroidal n , $|n| \leq 25$, a maximum of 19 poloidal side bands are centred around the poloidal m for which $n/m \approx \iota = 3/4$. This Fourier filter is used for the potentials on each of the 128 flux surfaces. Together with this resonance-condition aligned diagonal filter the Fourier solver implemented in EUTERPE is used.

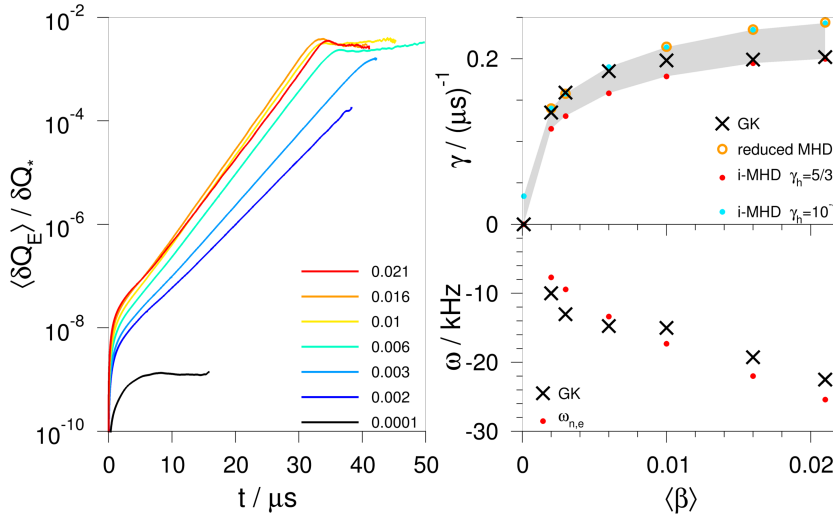


FIGURE 4. The β -sequence for the $\ell = 1, 2$ case (left panel of figure 1). Left: time evolution of the volume-averaged perturbed ion energy flux, $\langle \delta Q_E \rangle$, in normalised units, colours for plasma- β , $10^{-4} \leq \langle \beta \rangle \leq 0.021$ (black to red). Top right: growth rates, γ , versus $\langle \beta \rangle$: GK linear phase \times , linearised ideal MHD \bullet , with compressible ($\gamma_h = 5/3$, red) and nearly incompressible modes ($\gamma_h = 10^{-4}$, cyan) and incompressible reduced-MHD modes ($\gamma_h = 0$, orange \circ). The shading shows the range of the MHD growth rates. Bottom right: frequencies, ω , versus $\langle \beta \rangle$: GK \times , diamagnetic-drift frequency \bullet (red).

The GK simulations use 150 million ion markers, twice as many electron markers and Maxwellian equilibrium distribution functions for each species. The electron distribution function is shifted by a bulk velocity depending on all three position-space coordinates, in this way allowing for an equilibrium current. Realistic electron mass is used throughout this work. The equilibrium quantities are available on a cylindrical grid with sizes $300 \times 300 \times N_\varphi$ in (R, Z, φ) directions. With N_φ up to 2048, the aspect ratio of the mesh cells (the ratio of a cell's longest to its shortest length) is $N_\varphi/N_R \lesssim 2$. If not indicated otherwise, the GK simulations include the δB_{\parallel} term, equation (4.1).

Random initial conditions for δf are the standard choice. As a second option available in the EUTERPE code, $\delta \Phi$ is initialised as a superposition of two Fourier components with a Gaussian radial dependence. Since the present work focuses on specific low- m MHD modes, the latter option is used with one exception, which is discussed in § 6.2.1. If not stated otherwise, $(4, -3)$ and its tokamak-type side band $(3, -3)$ with half the amplitude were used with the Gaussians centred around $\rho = 0.75$.

6. Results

6.1. Comparison of linear-phase gyrokinetic and linear ideal-MHD stability results

In this section, the linear-phase properties of the nonlinear EUTERPE simulations, i.e. growth rates, frequencies and spatial structures, are compared with linear-ideal-MHD stability results. In the figures, the full time traces of the GK simulations are shown. The discussion of the nonlinear phase is given in § 6.2.

The GK growth rates are obtained from the volume-averaged perturbed ion energy flux (with m_p the proton mass)

$$\langle \delta Q_E \rangle = \frac{1}{V} \int \frac{m_p}{2} v^2 \delta f \frac{d \delta R}{dt} \cdot \frac{\nabla s}{|\nabla s|} d^3 x d^3 v. \quad (6.1)$$

Being quadratic with respect to the perturbation, this quantity grows with twice the growth rate γ (Mishchenko *et al.* 2021). In equation (6.1), V is the toroidal simulation volume.

Since the ideal-MHD force operator, equation (3.2), is Hermitian, its spectrum is real and corresponds to either pure oscillations, $\omega^2 > 0$, or unstable, growing modes, $\omega^2 < 0$. Hence, the ideal-MHD model does not provide frequencies for unstable perturbations. This fact again illustrates that ideal MHD is physically less complete than GK. However, as shown below in §§ 6.1.1 and 6.1.2, the electron diamagnetic-drift frequency (where e the elementary charge and ρ the radius)

$$\omega_{n,e} = \frac{1}{2} \omega_{p,e} = \frac{T_e m}{e B L_n \rho}, \quad (6.2)$$

proved to be in excellent agreement to the frequencies found in the GK simulations. In contrast to the general case, here $\omega_{n,e} = 1/2 \omega_{p,e}$, because the normalised profiles coincide.

6.1.1. Plasma- β sequence in $\ell = 1, 2$ cases

The left panel of figure 4 shows the existence of a clear linear phase in the evolution of $\langle \delta Q_E \rangle$ and the dependence of this quantity on the volume-averaged plasma- β for the β -scan of $\ell = 1, 2$ equilibria described in § 2. In the top right panel, the GK growth rates are compared with reduced-MHD CKA and ideal-MHD CAS3D stability results. The latter are calculated in two ways differing in the value of the ratio of the specific heats, γ_h , in the fluid compression, see equation (B.1): with the usual $\gamma_h = 5/3$ and with $\gamma_h = 10^{-4}$ as an approximation of reduced MHD. Since fluid compression always acts as stabilising, the growth rates calculated with non-zero γ_h are smaller than those of the reduced MHD. The GK growth rates are found within the interval created by the MHD growth rates. For $\langle \beta \rangle < 0.01$, the GK simulations yield growth rates that are in very good agreement with nearly incompressible ideal MHD and reduced MHD. Only if the plasma- β is large enough, i.e. for $\langle \beta \rangle \geq 0.01$, the GK growth rates agree very well with those obtained from the ideal-MHD calculations with $\gamma_h = 5/3$. In units of inverse Alfvén time, equation (2.6), the growth rates increase to $\gamma \tau_A \approx 0.054$ at $\langle \beta \rangle = 0.021$. As is shown in the bottom right panel of figure 4, the electron diamagnetic-drift frequency, equation (6.2), and the frequencies determined from the EUTERPE data compare well, so that the dependence on the plasma- β is correctly captured.

For a comparison of the spatial structures a point in time is chosen in the fully developed linear phase of the GK simulation, e.g. $t \approx 23.7 \mu s$ for the $\ell = 1, 2$ equilibrium at $\langle \beta \rangle = 0.016$. As is evident from equations (4.3) and (4.4), only the component of the ideal MHD displacement which is normal to the unperturbed magnetic surfaces is needed for the link to GK. As shown in figure 5, very good agreement is found for the Fourier harmonics of $\delta \Phi$ and δA_{\parallel} . In addition to the treatments in MHD and GK, the small deviations may also stem from the usage of different straight-field-line coordinates. In EUTERPE the so-called PEST coordinates (Grimm *et al.* 1976) are employed, which keep the angle φ of the cylindrical coordinates with planar toroidal cuts of the simulation domain. With the coordinates

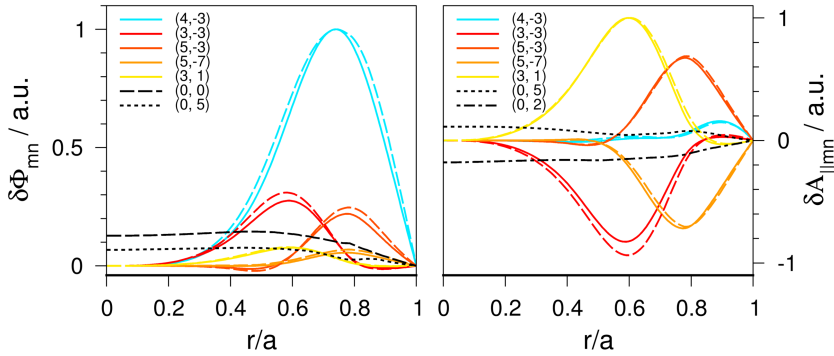


FIGURE 5. Dominant Fourier harmonics of $\delta\Phi$ (left) and δA_{\parallel} (right) at $t \approx 23.7 \mu\text{s}$ for the $\ell = 1, 2$ equilibrium at $\langle\beta\rangle = 0.016$. The ideal-MHD results (solid lines, $\gamma_h = 5/3$), are compared with the GK results (dashed). Colour legend: resonant $(4, -3)$ harmonic (cyan), toroidicity- (red) and helicity-induced side bands (orange, yellow). The $m = n = 0$ (zonal) and other $m = 0, n \neq 0$ components are only included in the GK simulation; $(0, 0)$ (black dashed), $(0, 5)$ (black dotted) and $(0, 2)$ (black dash-dotted).

used in CAS3D, however, the field lines and their orthogonals are straight and, hence, toroidal cuts are non-planar (Boozer 1982). Usually, the resulting differences are small. For clarity in the figure, only the strongest seven out of 597 harmonics are included. In $\delta\Phi$, the resonant harmonic, $(m, n) = (4, -3)$, is dominant being followed in amplitude by toroidal, tokamak-type side bands, $\Delta(m, n) = \pm(1, 0)$, and helical side bands, $\Delta(m, n) = \pm(1, -4)$ for the four-period stellarator. Due to the discrete, fourfold symmetry of the stellarator, the eigenmodes belonging to different mode families decouple in the MHD stability calculations (Schwab 1993). Therefore, the zonal component, $m = n = 0$, does not contribute to the dominantly $(4, -3)$ ideal-MHD perturbation. In contrast to the Fourier structure of $\delta\Phi$, the resonant harmonic of δA_{\parallel} , i.e. $(m, n) = (4, -3)$, is smaller than the toroidicity- and helicity-induced couplings, i.e. $(4, -3) \pm (1, 0)$ and $(4, -3) \pm (1, -N_p)$. This can be understood by a closer look on equations (4.3) and (4.4) employing magnetic coordinates, because then the directional derivatives ($\mathbf{B} \cdot \nabla$ and $\nabla s \times \mathbf{B} \cdot \nabla$) are linear differential operators in the magnetic angles with coefficients constant on flux surfaces. Therefore, additionally, this is conveniently done in Fourier space. It is seen that, firstly, the Fourier harmonics of $\delta\Phi$ only differ from the ones of the MHD normal displacement by a factor depending on the flux label. Secondly, ignoring the variations of B for a moment, the harmonics of δA_{\parallel} are analogously obtained from the Fourier harmonics of $\xi \cdot \nabla s$, however, multiplied by a factor $m\iota + n$, which approximately vanishes for resonant harmonics.

As described in § 2, throughout the present work identical normalised equilibrium temperature and density profiles were used. However, the decomposition of the equilibrium pressure profile into temperature and density profiles is arbitrary. Therefore, in addition to the $\eta_{i,e} = 1$ equilibrium profiles, simulations were also done for an $\ell = 1, 2$ equilibrium with the pressure of the $\eta_{i,e} = 1$ case being split into steep equilibrium temperature profiles, $T_e = T_i$, and flat, but non-uniform equilibrium density profiles, $n_e = n_i$, as shown in the left panel of figure 6. As illustrated in the middle panel, the linear-phase growth rate is lower for the flat-density simulation, $\gamma = 0.16 (\mu\text{s})^{-1}$, as compared with the one employing the $\eta_{e,i} = 1$ profiles, $\gamma = 0.2 (\mu\text{s})^{-1}$. The ideal-MHD stability calculations employing $\gamma_h = 5/3$,

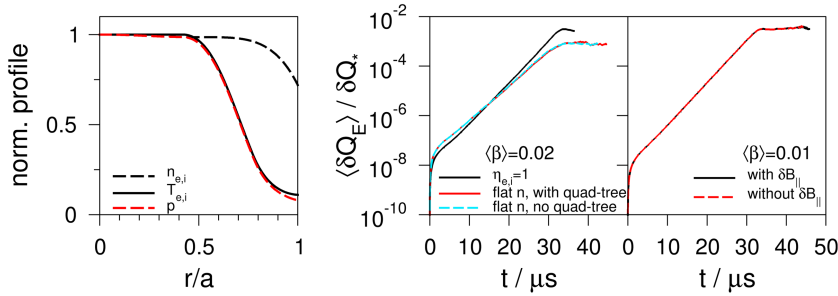


FIGURE 6. Left: normalised temperature (solid black), density (dashed black) and pressure (dashed red) equilibrium profiles of a flat-density scenario; compare figure 3 for the $\eta_{i,e} = 1$ profiles. Time evolution of the volume-averaged perturbed ion energy flux in normalised units for the $\ell = 1, 2$ case at $\langle \beta \rangle = 0.02$ (middle) and 0.01 (right). Middle panel: $\eta_{i,e} = 1$ (black), flat-density simulation with quad-tree smoothing (red), and without smoothing (cyan). Right panel: simulations including the $\delta B_{||}$ -terms (black) and omitting them (red).

however, find a slightly higher growth rate, $\gamma = 0.22 (\mu s)^{-1}$ for the flat-density case as compared with the $\eta_{i,e} = 1$ case with $\gamma = 0.2 (\mu s)^{-1}$. One reason for this may lie in a structural difference between ideal MHD and GK. The MHD force operator includes the equilibrium pressure and its gradient, and the equilibrium density only appears in the kinetic energy acting as a normalisation. Conversely, in GK the density and temperature gradients are both sources of free energy.

Comparative EUTERPE simulations including and omitting $\delta B_{||}$ are presented in the right panel of figure 6. With practically identical time traces, coincidence as well in the linear-phase growth rate as in the saturation level is found. Therefore, this term plays a subordinate role only, suggesting that it may be neglected in GK simulations in the regime of MHD proper. Here, the latter is understood as a scenario in which low- m and, therefore, spatially large-scale, modes are dominant. This finding is in line with Kennedy *et al.* (2024), where it was demonstrated that $\delta B_{||}$ has a large impact on hybrid-kinetic-ballooning mode (hybrid-KBM) stability at high β' (e.g. $\beta' = d\beta/d\rho \approx -0.5$ in their local GK simulations), and a negligible impact at lower β' . The latter case appears to apply in the simulations presented here, since β' is roughly five times smaller, $\beta' \approx -0.1$ at the location of the strongest pressure gradient, $\rho \approx 0.7$ (figure 3).

6.1.2. Vacuum-field magnetic-well sequence in HELIAS cases

The set of HELIAS equilibria described in § 2 is even more important because the geometry of the cases is more like W7-X, and information can be obtained on the vacuum-field magnetic well which is used as a series parameter. As shown in figure 7, the linear-ideal-MHD results and the linear-phase findings of the nonlinear GK simulations agree equally well. Both models find that a vacuum-field anti-well corresponds to instability. In units of inverse Alfvén time, equation (2.6), the growth rates increase from 0.015 to 0.033 for an increase of \mathcal{W}_{vf} from 0.006 to 0.03. As seen before, the electron diamagnetic-drift frequency, equation (6.2), is a good approximation to the frequencies determined by the GK simulations. During a EUTERPE simulation the relative magnetic-field perturbation normal to the unperturbed flux surfaces, hence δB^s , is monitored at selected times as illustrated by black bullets in

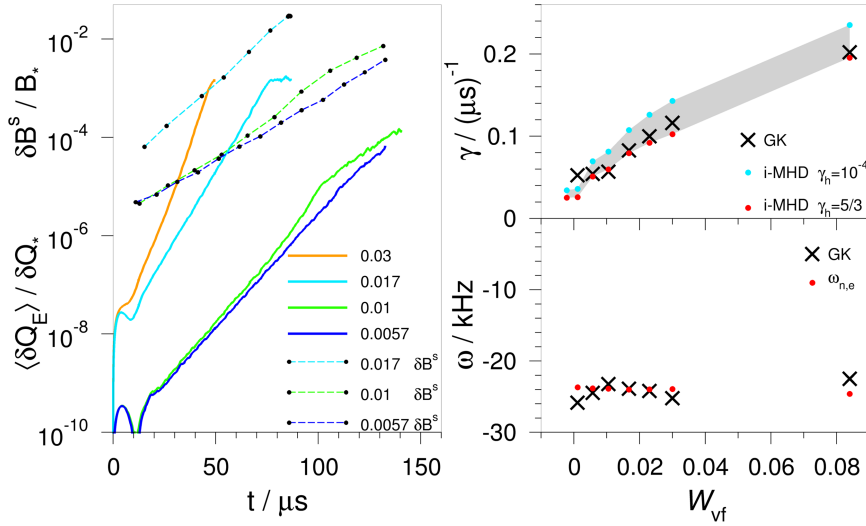


FIGURE 7. Sequence of HELIAS equilibria (right panel of figure 1) with variation of the vacuum-field magnetic anti-well, W_{vf} , at fixed $\langle \beta \rangle = 0.02$. Left: time evolution of the volume-averaged perturbed ion energy flux, $\langle \delta Q_E \rangle$, and of the magnetic-field perturbation, δB^s , both in normalised units. Colours indicate $W_{vf} = 0.0057, 0.01, 0.017, 0.03$ (blue, green, cyan, orange). Except for the latter case, the field perturbation is shown by \bullet with the dashed lines meant to guide the eye. Top right: growth rates, γ , versus vacuum-field magnetic anti-well, W_{vf} . From the GK linear phase \times and from linearised ideal MHD \bullet , with compressible ($\gamma_h = 5/3$, red) and nearly incompressible modes ($\gamma_h = 10^{-4}$, cyan). The shading shows the range of the MHD growth rates. Bottom right: frequencies, ω , versus W_{vf} : GK \times , diamagnetic-drift frequency \bullet .

the left panel of figure 7. It is defined by

$$\max_{s, \theta, \phi} \left| \frac{\nabla s}{|\nabla s|} \cdot \delta \mathbf{B} \right| / B_*, \quad (6.3)$$

with (s, θ, ϕ) extending over the total simulation domain, i.e. the torus in the present work. The EUTERPE code uses dimensionless quantities, B_* normalises the magnetic field (Appendix E and table 2). For $\langle \beta \rangle = 0.02$ and $W_{vf} = 0.017$ (cyan time traces), the relative field perturbation increases to 0.013 at the end of the linear phase, $t = 76 \mu s$, and saturates at ≈ 0.025 near the end of the simulation, $t = 86 \mu s$. It should be noted that the magnetic-field perturbation saturates with a time delay as compared with $\langle \delta Q_E \rangle$.

6.2. Analysis of the gyrokinetic results

6.2.1. Time evolution of energy fluxes, power spectra and profiles

In addition to the perturbed ion energy flux used in figure 4, figure 8 shows the time evolution of the volume-averaged total ion energy flux ($\langle Q_{E,0} \rangle$ is the unperturbed flux, which ideally should be zero, but can fluctuate due to particle noise in the PIC method) $\langle Q_E \rangle = \langle Q_{E,0} \rangle + \langle \delta Q_E \rangle$, for the plasma- β scan of $\ell = 1, 2$ stellarators. In all EUTERPE simulations discussed in this paper, in equilibrium $T_e(t_0 = 0) = T_i(t_0 = 0)$ and $n_e(t_0 = 0) = n_i(t_0 = 0)$, as described in § 2. Although they are independent quantities and independently evolving during the GK simulation, each type of profile

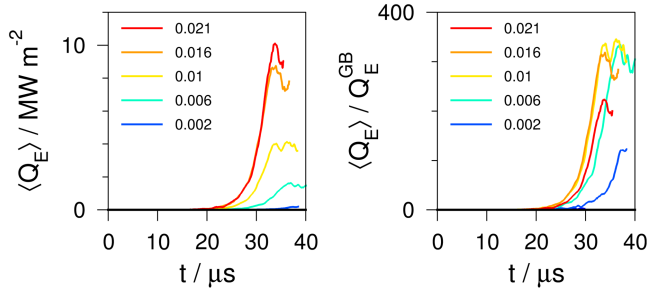


FIGURE 8. Time evolution of the volume-averaged total ion energy flux, $\langle Q_E \rangle = \langle Q_{E,0} \rangle + \langle \delta Q_E \rangle$, in SI (left) and gyro-Bohm units (right) in the $\ell = 1, 2$ case of figure 4; colours for plasma- β , $0.002 \leq \langle \beta \rangle \leq 0.021$.

(temperature and density) was found to evolve identically for ions and electrons in the scenarios studied here. Therefore, the energy fluxes are the same for electrons and ions (protons) in SI units. Given in gyro-Bohm units, they differ by a factor of $\sqrt{m_p/m_e}$. For $\langle \beta \rangle = 0.02$, the maximum of $\langle Q_E \rangle$ is reached at $\approx 32 \mu\text{s}$. For lower plasma pressures the maxima occur at slightly later points in time. Using SI units, it is seen that the saturation levels scale with the plasma pressure. They are comparatively high, e.g. ≈ 300 in gyro-Bohm units, due to the strongly unstable nature of the $\ell = 1, 2$ configuration.

Test simulations confirmed the necessity of keeping terms quadratic in the perturbed quantities in the equation of motion for u_{\parallel} , equation (C.6). Without these so-called magnetic-flutter terms saturation was not reached. The quadratic terms appear where derivatives along directions involving the magnetic field, $\mathbf{B} + \delta \mathbf{B}_{\perp}^{\text{GK}}$, are applied to perturbation quantities.

Furthermore, the influence of the so-called quad-tree smoothing for noise control (Sonnendrücker *et al.* 2015) was studied. For the flat-density $\ell = 1, 2$ case at $\langle \beta \rangle = 0.02$, GK simulations were performed with and without the smoothing option. As seen in the middle panel of figure 6, the smoothing procedure leads to an only slightly prolonged saturation phase in this specific case.

As described in § 6.1, modes detected in the GK simulations are said to have MHD signatures, if they are unstable with dominantly low- m partial modes and, hence, spatially global structures. Furthermore, they have negative GK frequencies, in good agreement with the electron diamagnetic-drift frequency and rotate in the electron diamagnetic direction. An important point of this work was to check how sub-dominant these MHD-like modes are compared with other modes present in the GK simulations. To this end, the initial conditions of $\delta \Phi$ employed for the EUTERPE simulations were varied. The GK results were then analysed using the time traces of the radially averaged power spectra for the Fourier harmonics of $\delta \Phi$

$$P_{mn}^{\Phi}(t) = \int_0^1 |\delta \Phi_{mn}(\rho, t)|^2 d\rho. \quad (6.4)$$

(The EUTERPE code uses normalised quantities which are derived from equilibrium quantities, Appendix E and table 2. A typical normalisation value for $\delta \Phi$ is

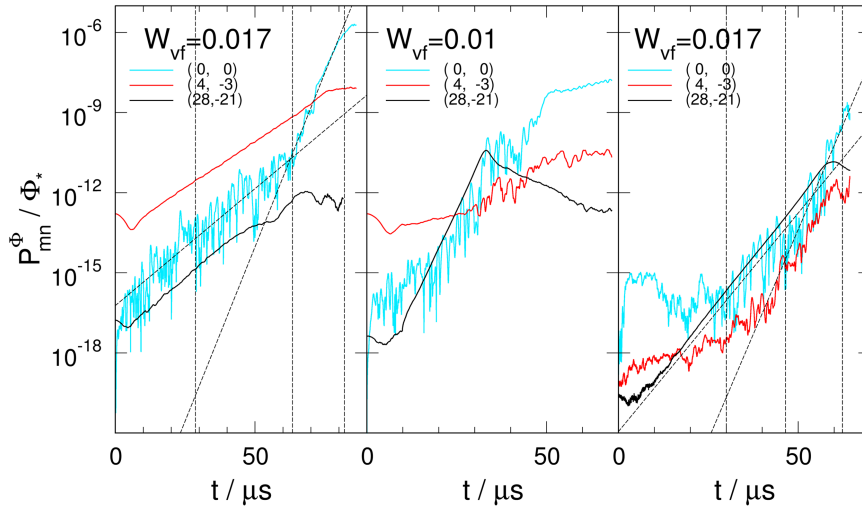


FIGURE 9. Time evolution of selected components of the $\delta\Phi$ power spectrum in normalised units, $\Phi_* = (\delta\Phi_*)^2$, shown for HELIAS equilibria at $\langle\beta\rangle = 0.02$, $\mathcal{W}_{vf} = 0.017$ (left, right) and $\mathcal{W}_{vf} = 0.01$ (middle). Left (middle): initialisation of $\delta\Phi$ with resonant mode $m = 4$, $n = -3$ and an admixture of $(28, -21)$ at a relative amplitude of 0.001 (0.005); right: initialisation with noise. Colour legend: low- m component $(4, -3)$ (red), high- m $(28, -21)$ (black), zonal component $(0, 0)$ (cyan). Vertical dashed lines indicate time intervals in which growth rates of the $(0, 0)$ component are determined by regression as shown by the diagonal dashed lines.

$\delta\Phi_* \approx 1500$ V.) By way of example, the four-period HELIAS case at $\langle\beta\rangle = 0.02$ and $\mathcal{W}_{vf} = 0.017$ and 0.01 is studied. The respective GK results are summarised in [figure 9](#). In a GK simulation started from noise, i.e. from a randomly set small initial perturbation, the linear phase is dominated by a high- m perturbation, $m = 28$, $n = -21$, its side bands, a toroidicity-coupled side band, $(27, -21)$, being the most important one. Other high- m resonant partial modes, e.g. $(24, -18)$ and $(22, -17)$, also contribute, with smaller, but comparable, amplitudes. The respective selected time traces of the total ion energy flux are shown in the right panel of [figure 9](#). With positive frequency, i.e. rotation in the ion-diamagnetic direction and strong amplitudes on the outside of the torus, the high- m mode has characteristics of a KBM (Aleynikova *et al.* 2018; Ishizawa *et al.* 2019). If, as the second choice, the simulation is explicitly initialised at low mode numbers, in this case the resonant $(4, -3)$, together with a small high- m content, here $(28, -21)$ at a relative amplitude of 0.001, then the MHD-type low- m mode is dominant in the simulation. The high- m component also grows (even at a slightly larger growth rate), but stays subdominant during the entire simulation, because of the much lower initial level. The respective selected time traces are shown in the left panel of [figure 9](#). For these two simulations (left and right panels of [figure 9](#)), the time traces of the total ion energy flux are shown in [figure 10](#). The low- m MHD-type mode (left panel of [figure 9](#)) reaches an ≈ 7.5 times higher maximum of $\langle\delta Q_E\rangle$ than the high- m KBM (right panel of [figure 9](#)). A third choice of initial conditions is illustrated in the middle panel of [figure 9](#). Compared with the low- m partial mode, $(4, -3)$, the relative amplitude of the high- m partial mode, $(28, -21)$,

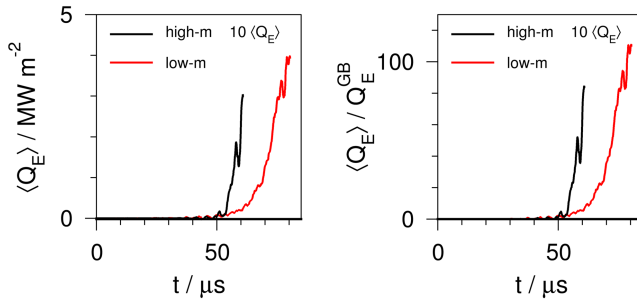


FIGURE 10. Time evolution of the volume-averaged total ion energy flux, $\langle Q_E \rangle = \langle Q_{E,0} \rangle + \langle \delta Q_E \rangle$, in SI (left) and gyro-Bohm units (right) for the simulations shown in the left (low- m) and right (high- m) panels of figure 9; HELIAS case at $\mathcal{W}_{\text{vf}} = 0.017$ and $\langle \beta \rangle = 0.02$. The values for the high- m results (black) are magnified by a factor 10.

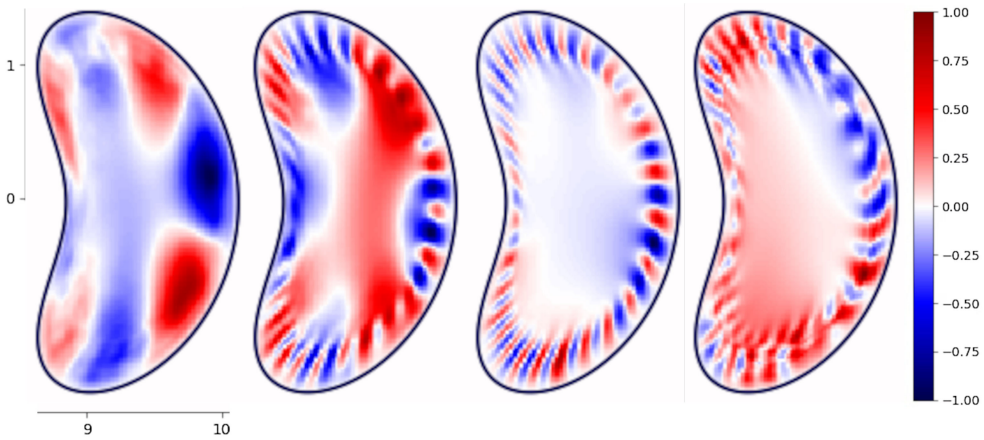


FIGURE 11. Time evolution of the $\delta\Phi$ contours in normalised units on the bean-shaped cross-section of the HELIAS equilibrium with $\mathcal{W}_{\text{vf}} = 0.01$ and $\langle \beta \rangle = 0.02$. Initialisation of $\delta\Phi$ with resonant mode $m = 4, n = -3$ and an admixture of $m = 28, n = -21$ with a relative amplitude of 0.005 (see middle panel of figure 9). Time points from left to right: $t / (\mu\text{s}) = 14, 21, 29, 36$.

is 0.005 at the start of the simulation, i.e. initially five times larger than in the simulation depicted in the left panel of figure 9. With this choice, however, the $(28, -21)$ KBM share outweighs the $(4, -3)$ MHD one at $\approx 25 \mu\text{s}$ towards the end of the linear phase. This third scenario is also illustrated in figure 11. A sequence of snapshots of $\delta\Phi$ contours on the bean-shaped cross-section shows how the initially MHD-type low- m mode transforms into a high- m KBM after an intermediate phase, in which the mode is a superposition of both contributions with practically no rotation. The KBM structures get sheared and eventually (while decaying in the saturation phase) become subdominant to zonal structures that dominate the simulation at later times (the latter not shown in figure 11).

Figure 12 shows the temporal evolution of the temperature and density profiles during the EUTERPE simulation for the HELIAS equilibrium at $\mathcal{W}_{\text{vf}} = 0.017$ and $\langle \beta \rangle = 0.02$, more specifically for a scenario with an unstable, low- m , spatially

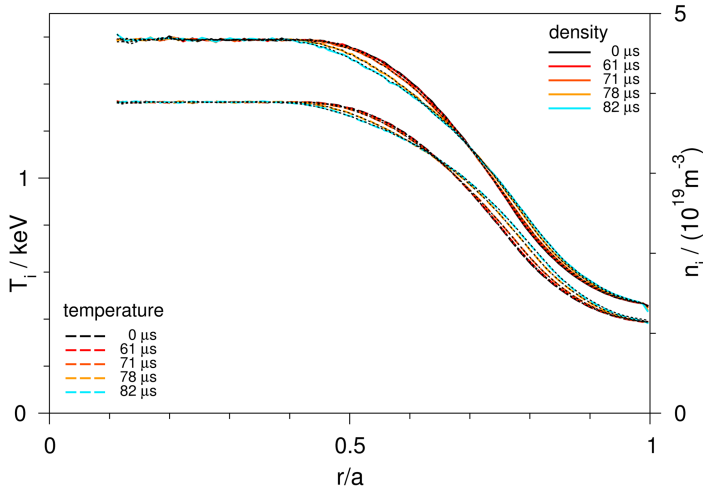


FIGURE 12. Time evolution of the profiles: ion temperature (coloured dashed) and ion density (coloured solid) in the HELIAS equilibrium at $\mathcal{W}_{\text{vf}} = 0.017$ and $\langle \beta \rangle = 0.02$. The respective electron profiles are shown as black dotted lines. The corresponding changes in the magnetic-field structure are shown in figure 14. Time ranges from $t = 0 \mu\text{s}$ (black) to $t \approx 82 \mu\text{s}$ (cyan). Intermediate time instances are shown in red to orange colours, $t = 61, 71, 78 \mu\text{s}$.

global and, hence, MHD-type mode. Initially, all normalised profiles are identical, $\eta_{i,e} = 1$. During the GK simulation, the temperatures and the densities evolve separately, however, identically for ions and electrons, i.e. for all times $T_e = T_i$ and $n_e = n_i$. Likewise, the ion and electron heat fluxes evolve identically in this scenario. The changes seen in the profiles are rather weak, mostly occurring in the early saturation phase, $t \lesssim 78 \mu\text{s}$. Flattening is seen inside, and, hence, a steepening outside the radial location of the strongest pressure gradient, $\rho \approx 0.7$.

6.2.2. Properties of the zonal flow

The role of $m = 0$ or zonal components is not yet clear and remains under investigation. They immediately appeared in all GK simulations for the MHD-unstable equilibria studied here. The time traces of $\langle \delta Q_E \rangle$, e.g. in figures 4 and 7, show that these simulations could not be continued deep into the saturation phase. A possible reason is seen in the eventual excessive growth of the zonal components during the saturation phase of the other modes, which leads to numerical problems and, consequently, the termination of the simulation. All computational parameters of the GK simulations were carefully checked, e.g. a smaller time step did not solve the problem. The various time traces only cover simulation phases with well-resolved and well-behaved Fourier harmonics of the perturbed potentials, $\delta\Phi$ and δA_{\parallel} . By way of example, the time traces of the power spectrum of $\delta\Phi_{0,0}$ are additionally shown in figure 9. In the simulations initialised with noise (right panel), and the low- m MHD-type perturbation (left panel), the $(0, 0)$ component oscillates and on average grows at the rate of the dominant mode as indicated by dashed lines. Towards the end of the linear phase, however, the $(0, 0)$ growth rate changes by a factor of approximately three in the MHD-type regime. In the KBM regime that developed from initial noise, a growth rate twice as high as for the KBM is found. Through this continuing increase of the zonal component the saturation phase ends

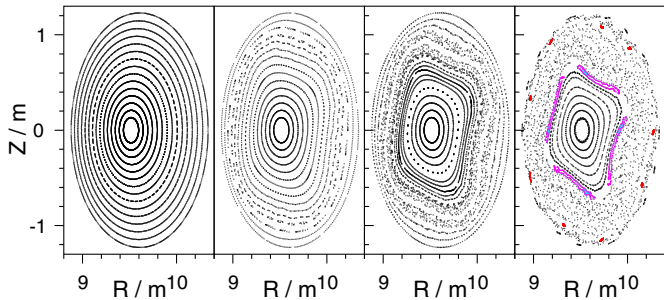


FIGURE 13. Field-line tracing for the GK magnetic field, $\mathbf{B} + \delta\mathbf{B}^{\text{GK}}(t)$, of the $\ell = 1, 2$ stellarator, [figure 1](#), with $\langle\beta\rangle = 0.006$, at $t/(\mu\text{s}) = 0, 32, 35.6$, and 40 (left to right). Selected field lines in islands are highlighted (right): $m = 4$ (cyan and magenta) and $m = 9$ (red). The $\varphi = 0^\circ$ cross-section is shown.

early, even though the dominant non-zonal modes decrease in amplitude. In the third scenario (middle panel), on the other hand, in which the KBM overtakes the MHD mode, a prolonged saturation phase develops, in which the high- m content decreases, and the zonal component only slightly increases.

6.2.3. Spatial structures of gyrokinetic perturbation and field-line tracing

The GK simulations proceed from equilibrium calculations assuming nested magnetic surfaces. While an unstable perturbation develops in time, it perturbs the initially intact magnetic geometry too.

For the $\ell = 1, 2$ equilibrium with $\langle\beta\rangle = 0.006$, [figure 13](#) shows the upright-ellipse cross-section at four instances in time, starting with the unperturbed magnetic field. For this simulation the time trace of the perturbed ion energy flux is shown in the left panel of [figure 4](#) (cyan). In the linear phase, $t = 32 \mu\text{s}$, high- m islands develop in the outer half of the plasma domain. In the late linear phase, $t = 35.6 \mu\text{s}$, an $m = 4$ island develops and the outer magnetic surfaces begin to ergodise. In the saturation phase, at $t = 40 \mu\text{s}$, the $m = 4$ island is seen to act in a shielding way, it encloses intact surfaces. Outside the $m = 4$ island, ergodisation leaves only remnants of $m = 9$ island near the plasma edge.

[Figure 14](#) shows the intact flux surfaces of the HELIAS equilibrium with $\langle\beta\rangle = 0.02$ and $\mathcal{W}_{\text{vf}} = 0.017$, and the evolution of the $m = 4$ island by two snapshots, at $t = 61 \mu\text{s}$ and $71 \mu\text{s}$. It should be noted here that the equilibrium configuration was deliberately chosen such that no low-order islands exist and the assumption of nested surfaces made by the VMEC code is well justified. With a relative magnetic-field perturbation, equation (6.3), of 0.003 at $t = 61 \mu\text{s}$, a thin $m = 4$ island exists and the magnetic surfaces near the plasma boundary wiggle slightly. Near the end of the linear phase, at $t = 71 \mu\text{s}$ and a relative field perturbation of 0.008 , the surfaces inside the $m = 4$ island are still intact, the island width has increased, and ergodised surfaces fill the outer part of the domain. The ergodisation is, however, not complete, as shown by colouring the distinct field lines. Similar findings are reported for simulations using the nonlinear MHD codes JOREK (Ramasamy *et al.* 2024) and M3D – C1 (Zhou *et al.* 2024). In [figure 10](#), it is seen that the total ion energy flux strongly increases from $t \approx 70 \mu\text{s}$. Interestingly, this coincides with the phase of increasing ergodisation of the magnetic field. Future work will continue the study of the magnetic-field structures seen GK simulations in more detail. In addition

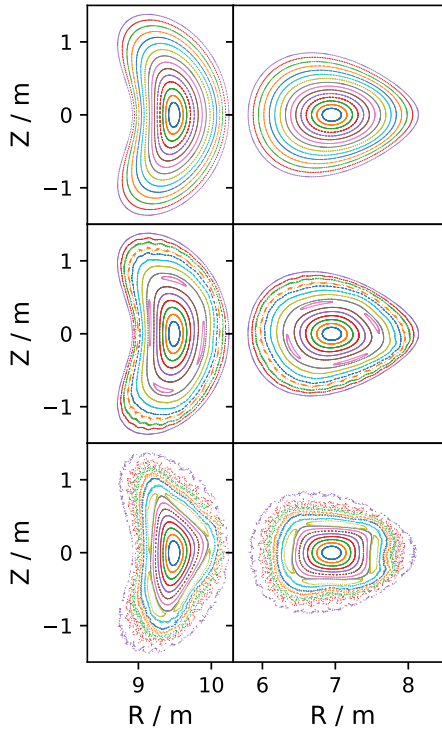


FIGURE 14. Field-line tracing for the GK magnetic field, $\mathbf{B} + \delta\mathbf{B}^{\text{GK}}(t)$, of the HELIAS stellarator with $\mathcal{W}_f = 0.017$, and $\langle\beta\rangle = 0.02$, at $t/(\mu\text{s}) = 0, 61$, and 71 (top to bottom). The $\varphi = 0^\circ$ (left) and 45° (right) cross-section are shown. Colours differentiate the field lines. Empty regions near the boundary indicate an island region.

to the magnetic islands, magnetic surfaces with highly irrational rotational transform (equivalent to Kolmogorov-Arnold-Moser (KAM) surfaces) and near-intact remnants of magnetic surfaces (so-called cantori) are of strong interest (Meiss 1992; Hudson & Breslau 2008). While the former are ‘immune’ against field perturbations and prevent complete ergodisation, the latter at least form partial barriers for field lines.

7. Summary and outlook

This work brings together GK and linear-ideal-MHD studies for helical-axis $\ell = 1, 2$ and HELIAS stellarators, the latter being the class of stellarators that also includes the W7-X configuration space. Electromagnetic, nonlinear simulations employing kinetic ions and kinetic electrons with physical mass ratio were performed with the EUTERPE GK code studying periodicity-breaking perturbations in the full toroidal plasma domain. Such simulations are the first of their kind, to the best knowledge of the authors. The linear-phase GK and the linear-ideal-MHD results were found to be in very good agreement: the growth rates and their dependence on the volume-averaged plasma- β and the vacuum-field magnetic well, as well as the Fourier structure of the perturbed electrostatic and parallel vector potentials of the modes. In particular, this means that both models find that a vacuum-field magnetic anti-well drives instability. It was shown that the parallel magnetic-field perturbation

plays no role in the GK simulation of the ideal-MHD-unstable equilibria that were studied in the present work. The inclusion of the magnetic-flutter term was found to be critical for reaching saturation in the GK simulation of the ideal-MHD-unstable equilibria. The sub-dominance of unstable low-mode-number MHD-type modes as compared with KBMs was confirmed in this type of low-shear stellarator. However, as shown by field-line-tracing, low-order island chains driven by the magnetic-field perturbation are expected. The islands enclose intact surfaces and are surrounded by ergodised surfaces in the outer plasma domain. Indications of increasing particle and energy fluxes seen in the present simulations after the onset of ergodisation (potentially leading to a loss of volume of good plasma confinement) will be studied in more detail in future work. In the saturation phase of the GK simulation, a slight flattening of temperature and density profiles was observed. It remains to be investigated whether the turbulent transport or the development of the island and ergodic regions is the cause of this flattening. The continued growth of the zonal-flow component in the saturation phase of the GK simulation will be the focus of future work as well as detailed studies of the magnetic-field structures arising in GK simulations. Similar simulations will evaluate the results of experiments conducted for a configuration with small vacuum-field magnetic anti-well in the OP2.3 operation campaign of W7-X.

Acknowledgements

Editor Paolo Ricci thanks the referees for their advice in evaluating this article.

Funding

This work has been carried out within the framework of the EUROfusion Consortium, funded by the European Union via the Euratom Research and Training Programme (Grant Agreement No 101052200 — EUROfusion). Views and opinions expressed are, however, those of the author(s) only and do not necessarily reflect those of the European Union or the European Commission. Neither the European Union nor the European Commission can be held responsible for them. The GK simulations presented in this work were performed on the MARCONI FUSION HPC system at CINECA contributing to the TSVVs Physics of Burning Plasmas and Stellarator Optimization of the EUROfusion work plan 2021-2025 and on the HPC systems Raven and Viper at the Max Planck Computing and Data Facility.

Declaration of interests

The authors report no conflict of interest.

Data availability

The data that support the findings of this article are available upon reasonable request from the authors.

Appendix A. Boundary of HELIAS configurations

In the VMEC equilibrium code, cylindrical coordinates, R , φ , Z , are employed with Fourier approximations for R and Z . The plasma boundary Fourier coefficients of the HELIAS configuration with marginal vacuum-field well are given in [table 1](#).

R_{mn}	0	1	2	Z_{mn}	0	1	2
-2		-0.01		-2		-0.01	
-1		-0.001		-1		-0.001	
0	8	0.9734	0.01	0	0	1.0266	0.01
1	0.856	-0.336	0.2	1	-0.69	0.336	0.2
2	0.11977	-0.0413	0.06	2	-0.11977	0.0413	-0.06

TABLE 1. Boundary coefficients of the HELIAS configuration with marginal vacuum-field magnetic well. In the rows, the poloidal index m increases, in the columns the toroidal index n .

In the boundary description for the case with $\mathcal{W}_{\text{vf}} = 0.03$ several coefficients are different, namely $R_{0,1} = 1.23$, $Z_{0,1} = -1.08$ and $R_{1,1} = -Z_{1,1} = -0.185$. The series of equilibria described in § 2 is obtained by interpolation of the boundary Fourier tables of these two limiting cases. For the $\ell = 1, 2$ case, all $m = 2$ coefficients (indentation and triangularity) are set to zero, the excursion of the magnetic axis strengthened by setting $R_{0,1} = 1.49$ and $Z_{0,1} = -1.3434$. The turning-ellipse coefficients remain at $-R_{1,1} = Z_{1,1} = 0.185$. Small adjustments of the rotational-transform profile were achieved by e.g. an increase in $-R_{1,1} = Z_{1,1}$ resulting in a positive shift of ι and a decrease in $R_{2,0} = Z_{2,0}$ which yields stronger shear.

Appendix B. Plasma potential energy of ideal MHD stability

A multitude of formulations were developed for the energy brought about by the ideal-MHD displacement ξ in the plasma, this energy being the most important part in the left-hand side of equation (3.2). The following representation, used e.g. by Correa-Restrepo (1978), explicitly separates stabilising and potentially destabilising terms

$$\begin{aligned}
 W_{\text{plasma}} = & \frac{1}{2} \int_{V_p} \left\{ B^{-2} |\mathbf{B} \times \delta \mathbf{B}|^2 + B^{-2} |\mathbf{B} \cdot \delta \mathbf{B} - \xi \cdot \nabla p|^2 + \gamma_h p |\nabla \cdot \xi|^2 \right. \\
 & + [(\xi \cdot \nabla p)(\kappa \cdot \xi^*) + (\xi^* \cdot \nabla p)(\kappa \cdot \xi)] \\
 & \left. - \frac{j_{\parallel}}{2B} [(\xi^* \times \mathbf{B}) \cdot \delta \mathbf{B} + (\xi \times \mathbf{B}) \cdot \delta \mathbf{B}^*] \right\} dV, \quad (\text{B.1})
 \end{aligned}$$

where $\delta \mathbf{B}$ is as in equation (3.1), the integration extends over the plasma domain and γ_h is the ratio of the specific heats. The field-line bending, the field compression and the plasma or fluid compression, in the order of the first line of equation (B.1), always contribute in favour of stability. The curvature, $\kappa = -\mathbf{b} \times (\nabla \times \mathbf{b}) = (\mathbf{b} \cdot \nabla) \mathbf{b}$, in combination with the equilibrium pressure gradient, and the equilibrium parallel-current density, $j_{\parallel} = \mathbf{j} \cdot \mathbf{b}$, may, however, give rise to pressure- and current-driven instabilities and may, therefore, have a detrimental effect on plasma stability.

Appendix C. Gyrokinetic equations of motion

For reference, the GK equations of motion are given here in the so-called mixed formulation used in the EUTERPE code. For each kinetic marker species, equations of motion are formulated. In this section the subscript for the marker species is omitted for clarity of notation. The scalar perturbed parallel vector potential δA_{\parallel} is

split into a symplectic and a Hamiltonian part

$$\delta A_{\parallel} = \delta A_{\parallel}^s + \delta A_{\parallel}^h. \quad (\text{C.1})$$

The Hamiltonian part, δA_{\parallel}^h , is used to define

$$u_{\parallel} \equiv v_{\parallel} + \frac{q}{m} \langle \delta A_{\parallel}^h \rangle, \quad (\text{C.2})$$

with $\langle \cdot \rangle$ denoting the gyro-average in the [Appendices C](#) and [D](#). The phase-space Jacobian is

$$B_{\parallel}^* = B + \left[\frac{m}{q} u_{\parallel} + \langle \delta A_{\parallel}^s \rangle \right] \mathbf{b} \cdot (\nabla \times \mathbf{b}). \quad (\text{C.3})$$

With the magnetic moment being a constant of motion, $\dot{\mu} = 0$, the evolution equation for v_{\perp} is

$$\dot{v}_{\perp} = \frac{v_{\perp}}{2B} \dot{\mathbf{R}} \cdot \nabla B. \quad (\text{C.4})$$

The equations of motion are

$$\begin{aligned} \dot{\mathbf{R}} = & u_{\parallel} \mathbf{b} + \frac{m}{q} \left[\frac{\mu}{B_{\parallel}^*} \mathbf{b} \times \nabla B + \frac{u_{\parallel}^2}{B_{\parallel}^*} \mathbf{b} \times \boldsymbol{\kappa} \right] - \frac{q}{m} \langle \delta A_{\parallel}^h \rangle \mathbf{b} \\ & + \frac{1}{B_{\parallel}^*} \mathbf{b} \times \nabla \langle \delta \Phi - u_{\parallel} (\delta A_{\parallel}^h + \delta A_{\parallel}^s) \rangle + \frac{m}{q} \frac{\mu}{B_{\parallel}^*} \mathbf{b} \times \nabla \delta B_{\parallel} \\ & + \frac{u_{\parallel}}{B_{\parallel}^*} (\langle \delta A_{\parallel}^s \rangle - \langle \delta A_{\parallel}^h \rangle) \mathbf{b} \times \boldsymbol{\kappa} \\ & + \frac{q}{m} \frac{1}{B_{\parallel}^*} \langle \delta A_{\parallel}^h \rangle [\mathbf{b} \times \nabla (\langle \delta A_{\parallel}^s \rangle + \langle \delta A_{\parallel}^h \rangle) - \langle \delta A_{\parallel}^s \rangle \mathbf{b} \times \boldsymbol{\kappa}] + \frac{1}{B_{\parallel}^*} \mathbf{b} \times \nabla \Phi_0, \end{aligned} \quad (\text{C.5})$$

and

$$\begin{aligned} \dot{u}_{\parallel} = & -\mu \nabla B \cdot \left[\mathbf{b} + \frac{m}{q} \frac{u_{\parallel}}{B B_{\parallel}^*} (\nabla \times \mathbf{B})_{\perp} \right] \\ & + \frac{q}{m} \frac{u_{\parallel}}{B_{\parallel}^*} \left[\mathbf{b} \times \nabla \langle \delta A_{\parallel}^h \rangle \cdot \nabla \langle \delta A_{\parallel}^s \rangle + (\langle \delta A_{\parallel}^s \rangle - \langle \delta A_{\parallel}^h \rangle) \mathbf{b} \times \boldsymbol{\kappa} \cdot \nabla \langle \delta A_{\parallel}^h \rangle \right] \\ & - \frac{\mu}{B_{\parallel}^*} \left[\mathbf{b} \times \nabla B \cdot \nabla \langle \delta A_{\parallel}^s \rangle + \frac{\langle \delta A_{\parallel}^s \rangle}{B} \nabla B \cdot (\nabla \times \mathbf{B})_{\perp} \right] \\ & + \frac{q}{m} u_{\parallel} \mathbf{b} \cdot \nabla \langle \delta A_{\parallel}^h \rangle - \frac{u_{\parallel}}{B_{\parallel}^*} \mathbf{b} \times \boldsymbol{\kappa} \cdot \nabla \langle \delta \Phi - u_{\parallel} \delta A_{\parallel}^h \rangle \\ & - \frac{q}{m} \frac{1}{B_{\parallel}^*} \left[\mathbf{b} \times \nabla \langle \delta \Phi \rangle \cdot \nabla \langle \delta A_{\parallel}^s \rangle + \langle \delta A_{\parallel}^s \rangle \mathbf{b} \times \boldsymbol{\kappa} \cdot \nabla \langle \delta \Phi \rangle \right] - \frac{q^2}{m^2} \langle \delta A_{\parallel}^h \rangle \mathbf{b} \cdot \nabla \langle \delta A_{\parallel}^h \rangle \\ & - \mu \left[\mathbf{b} + \frac{m}{q} \frac{u_{\parallel}}{B_{\parallel}^*} \mathbf{b} \times \boldsymbol{\kappa} \right] \cdot \nabla \delta B_{\parallel} - \frac{u_{\parallel}}{B_{\parallel}^*} \mathbf{b} \times \boldsymbol{\kappa} \cdot \nabla \Phi_0 \\ & + \frac{q}{m} \frac{1}{B_{\parallel}^*} \left[\mathbf{b} \times \nabla \langle \delta A_{\parallel}^s \rangle - \langle \delta A_{\parallel}^s \rangle \mathbf{b} \times \boldsymbol{\kappa} \right] \cdot \nabla \Phi_0. \end{aligned} \quad (\text{C.6})$$

$\langle\beta\rangle$	$p_0(0)$ /kPa	$T_{e,i}(0)$ /keV	$n_{e,i}(0)$ / 10^{20}m^{-3}	n_*	t_* / μs	v_* / ms^{-1}	B_* /T	$\delta\Phi_*$ /V	$\delta A_{\parallel*}$ /tm
0.021	25.973	1.516	0.5346	0.3605	0.0082	377465	1.2736	1487	0.004

TABLE 2. Magnetic-axis values of equilibrium profiles and normalisations used in the CAS3D and EUTERPE simulations for the $\ell = 1, 2$ stellarator of figure 1 with the maximum volume-averaged plasma- β used in the calculations.

In the above equations, (C.5) and (C.6), an externally given electrostatic potential Φ_0 describes the influence of a radial electric field.

Note that in the equations of motion terms quadratic in the perturbed field are retained because they are important for the nonlinear saturation of the modes.

Appendix D. Gyrokinetic weight and field equations in mixed formulation

In the following, the subscript $s = i, e$ denotes the marker species. The masses are normalised to the proton mass, the charges to the unsigned elementary charge

$$m_s = \frac{m_{i,e}}{m_p} \quad \text{and} \quad q_s = \frac{q_{i,e}}{|e|}. \quad (\text{D.1})$$

The weights w_s of the PIC marker particles evolve according to

$$\dot{w}_s = -\Omega_p S_s, \quad \text{with} \quad S_s = \dot{\mathbf{R}} \cdot \nabla f_{0,s} + \dot{u}_{\parallel} \frac{\partial f_{0,s}}{\partial v_{\parallel}} + \dot{v}_{\perp} \frac{\partial f_{0,s}}{\partial v_{\perp}}, \quad (\text{D.2})$$

with Ω_p the marker phase-space volume. The unperturbed distribution functions are

$$f_{0,s} = \frac{n_{0s}}{(2\pi)^{\frac{3}{2}} v_{\text{th},s}^3} \exp\left(-\frac{-u_{\parallel,s}^2 + v_{\perp,s}^2}{2 v_{\text{th},s}^2}\right), \quad (\text{D.3})$$

with the thermal velocities given by $v_{\text{th},s}^2 = T_s/m_s$. The perturbed electrostatic potential follows from the quasi-neutrality equation

$$\sum_s q_s n_s = 0, \quad n_s = \langle n_s \rangle + \frac{m_s}{q_s} \nabla \cdot \left(\frac{n_{0s}}{B^2} \nabla_{\perp} \delta\Phi \right). \quad (\text{D.4})$$

Ohm's law determines the symplectic part of δA_{\parallel}

$$\frac{\partial \delta A_{\parallel}^s}{\partial t} + \mathbf{b} \cdot \nabla \delta\Phi = 0. \quad (\text{D.5})$$

For a given symplectic δA_{\parallel}^s , the Hamiltonian part of δA_{\parallel} is determined by Ampère's law

$$-\frac{1}{\mu_0} \nabla \cdot \nabla_{\perp} \delta A_{\parallel}^h + \sum_s n_{0s} \frac{q_s^2}{m_s} \delta A_{\parallel}^h = \sum_s \langle j_{\parallel,s} \rangle + \frac{1}{\mu_0} \nabla \cdot \nabla_{\perp} \delta A_{\parallel}^s. \quad (\text{D.6})$$

A pressure balance equation is employed to calculate δB_{\parallel}

$$-\frac{B}{\beta_{\text{EU}}} \delta B_{\parallel} = \sum_s \delta p_{\perp,s}, \quad (\text{D.7})$$

with the perpendicular perturbed pressure given by

$$\delta p_{\perp s} = m_s \int \mu B \delta f_s B_{\parallel}^* du_{\parallel} d\mu d\alpha, \quad (\text{D.8})$$

and the quantity $\beta_{\text{EU}} = (\mu_0 k_B n_* T_*)/B_*^2$. The normalisations, indicated by the subscript $*$, are explained in the [Appendix E](#). The phase-space Jacobian B_{\parallel}^* is defined in equation (C.3). The angle α determines the direction of the gyro-radius vector on the gyro-disc.

Appendix E. Normalised units in the EUTERPE code

The EUTERPE code employs normalised units. The internal units are $\Omega_* = 1/t_* = |e|B_*/m_p$, with B_* the average value of the equilibrium magnetic field on the magnetic axis, $v_* = \rho_* \Omega_*$ for velocities, with $\rho_* = \sqrt{k_B T_* m_p}/(|e|B_*)$. The temperature T_* is the electron temperature at mid minor radius. The densities are normalised to the volume-averaged ion number density, $n_* = N_{\text{ph}}/V$, with V the volume of the toroidal plasma domain. Derived normalisation parameters are $\delta\Phi_* = k_B T_*/|e|$ for the perturbed electrostatic potential and $\delta A_{\parallel*} = \rho_* B_*$ for the perturbed parallel vector potential. The normalisation of the energy fluxes is done via $Q_{E*} = m_p n_* v_*^3$. The transformation to gyro-Bohm units is obtained from $Q_{E,s}^{\text{GB}} = m_s n_s v_s^3 (\rho_s/a)^2$, with a the effective minor radius of the toroidal plasma, and the subscript $s = e$ or i indicating the particle species. Typical values for the $\ell = 1, 2$ equilibrium of [figure 1](#) are summarised in [table 2](#).

REFERENCES

- ALEYNIKOVA, K., ZOCCO, A., XANTHOPOULOS, P., HELANDER, P. & NÜHRENBURG, C. 2018 Kinetic ballooning modes in tokamaks and stellarators. *J. Plasma Phys.* **84** (6), 745840602.
- BEIDLER, C.D. *et al.* 1990 Physics and engineering design for Wendelstein VII-X. *Fusion Technol.* **17** (1), 148–168.
- BERNSTEIN, I.B., FRIEMAN, E.A., KRUSKAL, M.D., KULSRUD, R.M. & CHANDRASEKHAR, S. 1958 An energy principle for hydromagnetic stability problems. *Proc. R. Soc. Lond. Series A. Math. Phys. Sci.* **244** (1236), 17–40.
- BOOZER, A.H. 1982 Establishment of magnetic coordinates for a given magnetic field. *Phys. Fluids* **25** (3), 520–521.
- BOOZER, A.H. 1984 Magnetic island growth. *Phys. Fluids* **27** (8), 2055–2062.
- BRIZARD, A.J. 1992 Nonlinear gyrofluid description of turbulent magnetized plasmas. *Phys. Fluids B: Plasma Phys.* **4** (5), 1213–1228.
- BRIZARD, A.J. & HAHM, T.S. 2007 Foundations of nonlinear gyrokinetic theory. *Rev. Mod. Phys.* **79** (2), 421–468.
- BROCHARD, G., *et al.* 2022 Verification and validation of linear gyrokinetic and kinetic-MHD simulations for internal kink instability in DIII-D tokamak. *Nucl. Fusion* **62** (3), 036021.
- COLE, M.D.J., HAGER, R., MORITAKA, T., DOMINSKI, J., KLEIBER, R., KU, S., LAZERSON, S., RIEMANN, J. & CHANG, C.S. 2019 Verification of the global gyrokinetic stellarator code XGC-S for linear ion temperature gradient driven modes. *Phys. Plasmas* **26** (8), 082501.
- CORREA-RESTREPO, D. 1978 Ballooning modes in three-dimensional MHD equilibria with shear. *Z. Naturforsch. A* **33** (7), 789–791.
- DEWAR, R.L. & HUDSON, S.R. 1998 Stellarator symmetry. *Physica D: Nonlinear Phenom.* **112** (1), 275–280.
- DINKLAGE, A. *et al.* 2018 Magnetic configuration effects on the Wendelstein 7-X stellarator. *Nat. Phys.* **14** (8), 855–860.

- DONG, G., BAO, J., BHATTACHARJEE, A., BRIZARD, A., LIN, Z. & PORAZIK, P. 2017 Gyrokinetic particle simulations of the effects of compressional magnetic perturbations on drift-Alfvénic instabilities in tokamaks. *Phys. Plasmas* **24** (8), 081205.
- DREVLAK, M., BEIDLER, C.D., GEIGER, J., HELANDER, P. & TURKIN, Y. 2018 Optimisation of stellarator equilibria with ROSE. *Nucl. Fusion* **59** (1), 016010.
- FREIDBERG, J.P. 2014 *Ideal MHD*. Cambridge University Press.
- GRAD, H. 1967 Toroidal containment of a plasma. *Phys. Fluids* **10** (1), 137–154.
- GREENE, J.M. 1997 A brief review of magnetic wells. *Plasma Phys. Control. Fusion* **17** (6), 389.
- GRIMM, R.C., GREENE, J.M. & JOHNSON, J.L. 1976 Computation of the magnetohydrodynamic spectrum in axisymmetric toroidal confinement systems. In *Controlled Fusion* (ed J. KILLEEN), Methods in Computational Physics: Advances in Research and Applications, vol. 16, pp. 253–280. Elsevier.
- HAIN, K., LÜST, R. & SCHLÜTER, A. 1957 Zur Stabilität eines Plasmas. *Z. Naturforsch. A* **12** (10), 833–841.
- HIRSHMAN, S.P., VAN RIJ, W.I. & MERKEL, P. 1986 Three-dimensional free boundary calculations using a spectral Green's function method. *Comput. Phys. Commun.* **43** (1), 143–155.
- HUDSON, S.R. & BRESLAU, J. 2008 Temperature contours and ghost surfaces for chaotic magnetic fields. *Phys. Rev. Lett.* **100** (9), 095001.
- ISHIZAWA, A., IMADERA, K., NAKAMURA, Y. & KISHIMOTO, Y. 2019 Global gyrokinetic simulation of turbulence driven by kinetic ballooning mode. *Phys. Plasmas* **26** (8), 082301.
- JOINER, N., HIROSE, A. & DORLAND, W. 2010 Parallel magnetic field perturbations in gyrokinetic simulations. *Phys. Plasmas* **17** (7), 072104.
- KENNEDY, D., GIACOMIN, M., CASSON, F.J., DICKINSON, D., HORNSBY, W.A., PATEL, B.S. & ROACH, C.M. 2023 Electromagnetic gyrokinetic instabilities in step. *Nucl. Fusion* **63** (12), 126061.
- KENNEDY, D., *et al.* 2024 On the importance of parallel magnetic-field fluctuations for electromagnetic instabilities in STEP. *Nucl. Fusion* **64** (8), 086049.
- KLEIBER, R., *et al.* 2024 EUTERPE: a global gyrokinetic code for stellarator geometry. *Comput. Phys. Commun.* **295**, 109013.
- MEISS, J.D. 1992 Symplectic maps, variational principles, and transport. *Rev. Mod. Phys.* **64** (3), 795–848.
- MERCIER, C. 1962 Critère de stabilité d'un système toroïdal hydromagnétique en pression scalaire. In *Plasma Physics and Controlled Nuclear Fusion Research* Nucl. Fusion Suppl., vol. 2, pp. 801. International Atomic Energy Agency.
- MISHCHENKO, A., BIANCALANI, A., BOTTINO, A., HAYWARD-SCHNEIDER, T., LAUBER, P., LANTI, E., VILLARD, L., KLEIBER, R., KÖNIES, A. & BORCHARDT, M. 2021 Numerics and computation in gyrokinetic simulations of electromagnetic turbulence with global particle-in-cell codes. *Plasma Phys. Contrrrol. Fusion* **63** (8), 084007.
- MISHCHENKO, A., KÖNIES, A., KLEIBER, R. & COLE, M. 2014 Pullback transformation in gyrokinetic electromagnetic simulations. *Phys. Plasmas* **21** (9), 092110.
- NÜHRENBURG, J., MERKEL, P., SCHWAB, C., SCHWENN, U., COOPER, A., HAYASHI, T., HIRSHMAN, S.P., JOHNSON, J.L., MONTICELLO, D.A. & REIMAN, A.H. 1993 MHD-theoretical aspects of stellarators. *Plasma Phys. Control. Fusion* **35** (SB), B115–B128.
- NÜHRENBURG, J. & ZILLE, R. 1986 Stable stellarators with medium β and aspect ratio. *Phys. Lett. A* **114** (3), 129–132.
- RAMASAMY, R., ALEYNIKOVA, K., NIKULSIN, N., HINDENLANG, F., HOLOD, I., STRUMBERGER, E., HOELZL, M. & the JOREK team 2024 Nonlinear MHD modeling of soft β limits in W7-AS. *Nucl. Fusion* **64** (8), 086030.
- SCHWAB, C. 1993 Ideal MHD: global mode analysis of three-dimensional plasma configurations. *Phys. Fluids B: Plasma Phys.* **5** (9), 3195–3206.
- SLABY, C., KÖNIES, A. & KLEIBER, R. 2024 A perturbative multi-mode model with finite parallel electric field for fast-ion-driven Alfvén eigenmodes. *Nucl. Fusion* **64** (12), 126016.
- SONNENDRÜCKER, E., WACHER, E., HATZKY, R. & KLEIBER, R. 2015 A split control variate scheme for PIC simulations with collisions. *J. Comput. Phys.* **295**, 402–419.

- WAELEBROECK, F.L. 2009 Theory and observations of magnetic islands. *Nucl. Fusion* **49** (10), 104025.
- WILMS, F., BAÑÓN NAVARRO, A., MERLO, G., LEPPIN, L., GÖRLER, T., DANNERT, T., HINDENLANG, F. & JENKO, F. 2021 Global electromagnetic turbulence simulations of W7-X-like plasmas with GENE-3D. *J. Plasma Phys.* **87** (6), 905870604.
- WILMS, F., BAÑÓN NAVARRO, A., WINDISCH, T., BOZHENKOV, S., WARMER, F., FUCHERT, G., FORD, O., ZHANG, D., STANGE, T. & the W7-X Team 2024 Global gyrokinetic analysis of Wendelstein 7-X discharge: unveiling the importance of trapped-electron-mode and electron-temperature-gradient turbulence. *Nucl. Fusion* **64** (9), 096040.
- ZHOU, Y., ALEYNIKOVA, K., LIU, C. & FERRARO, N.M. 2024 Benign saturation of ideal ballooning instability in a high-performance stellarator. *Phys. Rev. Lett.* **133** (13), 135102.
- ZOCCO, A., HELANDER, P. & CONNOR, J.W. 2015 Magnetic compressibility and ion-temperature-gradient-driven microinstabilities in magnetically confined plasmas. *Plasma Phys. Control. Fusion* **57** (8), 085003.